actuators
MDPI

Article

Robotic Knee Prosthesis with Cycloidal Gear and Four-Bar Mechanism Optimized Using Particle Swarm Algorithm

Mouaz Al Kouzbary [1], Hamza Al Kouzbary [1], Jingjing Liu [1], Taha Khamis [1], Zaina Al-Hashimi [1], Hanie Nadia Shasmin [1], Nooranida Arifin [1] and Noor Azuan Abu Osman [1,2,*]

[1] Center for Applied Biomechanics, Department of Biomedical Engineering, Faculty of Engineering, University of Malaya, Kuala Lumpur 50603, Malaysia
[2] The Chancellery, Universiti Tenaga Nasional, Kajang 43000, Malaysia
* Correspondence: azuan@um.edu.my

Abstract: A powered transfemoral prosthesis is needed as people with transfemoral amputation show 60 percent extra metabolic cost when compared to people with no amputation. Recently, as illustrated in the literature, the most high-torque robotic knee prosthesis utilize harmonic reducers. Despite the advantage of high reduction ratio and efficiency, the harmonic drive cannot be back-driven. Therefore, the harmonic drive is not an optimal solution for prosthetic systems with direct and indirect contact with the environment. In this paper, we outline an initial design of robotic knee prosthesis. The proposed robotic knee prosthesis consists of BLDC motor, cycloidal gear with reduction ratio 13:1, four-bar mechanism, and timing belt transmission with 4:1 reduction ratio. To optimize the torque transmission and range of motion (RoM), a multiobjective optimization problem must be undertaken. The end-effector motion depends on each bar length in the four-bar mechanism. The four-bar mechanism was optimized using particle swarm optimization (PSO). To complete the optimization, a set of 50 steps was collected using wearable sensors. Then, the data of sagittal plan were processed to identify the target profile for PSO. The prototype's computer-aided manufacturing (CAM) was completed using a MarkTwo 3D printer with carbon fiber composite. The overall design can achieve a maximum torque of 84 N.m. However, the current design lacks the elastic component (no spring is added on the actuator output), which is necessary for a functional prosthesis; this limitation will be addressed in future study.

Keywords: cycloidal drive; robotic knee joint; robotic prostheses; powered prostheses; cycloidal gear

Citation: Al Kouzbary, M.; Al Kouzbary, H.; Liu, J.; Khamis, T.; Al-Hashimi, Z.; Shasmin, H.N.; Arifin, N.; Abu Osman, N.A. Robotic Knee Prosthesis with Cycloidal Gear and Four-Bar Mechanism Optimized Using Particle Swarm Algorithm. *Actuators* **2022**, *11*, 253. https://doi.org/10.3390/act11090253

Academic Editors: Yuichi Kurita and Takayuki Tanaka

Received: 22 July 2022
Accepted: 29 August 2022
Published: 1 September 2022

1. Introduction

The knee complex is a limited condyloid joint. It consists of two joints with three degrees of freedom (DoF) (tibiofemoral and patellofemoral joints). Tibiofemoral joint functions mostly as a hinge joint with a slight rotation (i.e., adduction/abduction and internal/external), whereas patellofemoral joint main function is as a knee extension with the mechanical advantage of increasing the leverage of patellar tendon, which maximizes the knee torque [1]. Knee full-range of flexion is between 130° and 160°. However, in daily activities, the range drops to a value between 60° and 70° when walking, 80° while ascending stairs, and 90° from sitting to standing. Moreover, knee full-range of extension is 5° [1]. The knee joint's peak moment occurs at early stance [2]; the knee complex generates from 0.3 to 0.7 and 1.2 to 1.7 N.m/kg when walking and running, respectively. By establishing the requirements of torque and RoM, we can discuss the weight limitation for a functional robotic knee prosthesis.

Subatmospheric suspension can provide a vacuum range between 0 and −8 inHg. During the swing phase, the fictitious force acts on the socket [3]. Therefore, the momentum should be minimized by decreasing the prosthesis mass. The knee joint prosthesis weight would be between 0.5 and 1.6 kg. However, the size of the knee prosthesis is not critical for the design configuration.

In summary, a functional design of a single DoF robotic knee prosthesis must mimic the complementary function of the knee joint. The knee joint stiffness is high during stance phase and low during swing phase. Moreover, the knee net mechanical power increases dramatically with ambulation speed and during terrain changes. A functional robotic knee prosthesis should not only be able to provide the nonlinear stiffness, but also should be able to produce the necessary amount of torque for all types of daily activities.

All robotic prostheses with an electrical actuator are adopting permanent magnet motors as they are more efficient and have high-torque density [4]. The DC motor was selected because it has a linear relationship between torque and current, which makes the control system simple and inherently stable [5]. From Table 1, the actuators with BLDC motors can produce higher torque. However, the BLDC motor is not optimal for the application as the motor is not in a continuous high-speed operating mode [6].

As shown in Tables 1 and 2, most of the prototypes used a motor with 200 Watt nominal power. In recent years, more designs are using high-torque outrunner BLDC [7,8]. The new generation of powered prostheses can allow users to ambulate with a wider speed range and enhanced RoM, because the high-power motor can support the body during dorsiflexion.

Table 1. Powered ankle–foot prosthesis actuator design parameters.

Motor	Motor's Power (Watt)	Elastic Element(s)	Stiffness	
DC motor	150	Series spring	Flexion 300 kN/m Extension 600 kN/m	[9]
DC motor	150	Series and parallel springs	1200 kN/m (series) 770 kN/m (parallel)	[10]
BLDC motor	200	Series and parallel springs	600 kN/m (series) 630 Nm/rad (parallel)	[11]
BLDC motor	200	Series and parallel springs	1200 Nm/rad (series) 533 Nm/rad (parallel)	[12]
BLDC motor [1]	400	N/A	-	[13]
BLDC motor [1]	600	Series spring	378 kN/m	[7]
DC motor	150	Series and Nonlinear keel springs	32 kN/m (series)	[14]
DC motor	150	Series spring	50 kN/m (series)	[15]
DC motor	83	Series springs	500 kN/m (series) 200 kN/m (toe-spring)	[16]
BLDC motor	50	N/A	-	[17]
DC motor	150	N/A	-	[18,19]
BLDC motor	200	Parallel spring	43 Nm/rad	[20]
BLDC motor	200	Parallel spring	240 Nm/rad	[21]
DC motor	150	Series spring	26.6 Nm/rad	[22]
BLDC motor	200	N/A	-	[23]
DC motor	60	Series springs	120 kN/m (series) 300 kN/m (toe-spring)	[24]
DC motor	60	Series springs	60 kN/m (series) 300 kN/m (toe-spring)	[25]
BLDC motor	50	Series springs	180 kN/m(series) 300 kN/m (toe-spring)	[26]
DC motor	60	Series spring	132 kN/m	[27]
DC motor	60	Series and parallel springs	130 kN/m (series) 270 Nm/rad (parallel)	[28]
DC motor	90	Nonlinear parallel spring	No information given	[29,30]
BLDC motor	200	Series spring	445 kN/m	[31]
BLDC motor	283	Shock-absorber	No information given	[32]
DC motor	150	Series spring	208 kN/m	[33]
DC motor	150	Series springs	210 kN/m 42 Nm/rad (toe)	[34]

[1] outrunner.

Table 2. Transfemoral robotic prosthesis actuators.

Motor	Motor's Power (Watt)	Elastic Element(s)	Stiffness	
BLDC motor	200	Series spring for ankle actuator	38 kN/m	[35]
DC motor	150 (extension) 60 (flexion)	Series springs	160 Nm/rad 137 Nm/rad	[36]
DC motor	150	Series spring	200 Nm/rad	[37]
BLDC motor	200	No information	-	[38]
BLDC motor	200	Series springs	385 kN/m (extension) 338 kN/m (flexion)	[39]
BLDC motor	600	Series spring	378 kN/m	[7]
BLDC motor	483	N/A	-	[40]
BLDC motor	206	Torsion series springs	1146 Nm/rad	[41]
BLDC motor	400	Torsion series springs	600 Nm/rad	[8]
BLDC motor	410	-	-	[42]
BLDC motor	40	Series springs	17–974 Nm/rad	[43]
BLDC motor	240	-	-	[44]
BLDC motor	90	Shock absorber	No information given	[45]

Nonetheless, the utilization of BLDC motor is justifiable for the high torque-to-weight ratio. Finally, the PMSM can be potentially the best machine to develop actuators for robotic prostheses based on the motor characteristic [6].

As shown in Tables 1 and 2, the permanent feature of all prostheses is the elastic element(s), which can help in optimizing the device power production and consumption [46]. Furthermore, the elastic element of the design reduces the shocking load in every heel-strike event. Therefore, the elastic actuators are featured consistently in the field of robotic prostheses. The actuator output is connected to the end-effector via a mechanism that amplifies the torque and generates limits on the RoM.

In Tables 1 and 2, the consistency of the motor selection is noticeable. However, the elastic element of the actuators varies between 38 and 1200 kN/m [12,35]. The variation of the elastic elements can be attributed to the difference in working mechanisms and actuator structures. The ankle–foot stiffness is an important factor in ambulation metabolic cost [47]. In another study, it was found that the self-selected stiffness tends to increase the kinematics correlation between the biological limb and prosthetic limb with no noticeable effect on the metabolic cost [48]. Moreover, the increase in the stiffness above the self-selected stiffness led to reduction in metabolic cost and reduction in kinematic correlation [48]. This finding can answer the issue raised in [49], where the powered prosthesis' positive mechanical work is not the only source of metabolic cost.

The vast majority of powered prostheses use linkage mechanisms, and the stability of the linkage mechanisms has been well established through analysis [50,51]. The most common linkage mechanisms are slider-crank [52] and four-bar mechanism [8]. Other designs applied multistage transmission [41,53]. The nonlinear profile and variable transmission ratio are important factors on the mechanism selection.

Table 3 shows the commonly used mechanisms in robotic prostheses design; some systems were developed with the direct drive method. In order to achieve the design requirements, high-torque outrunner motors were used with harmonic gear, which can achieve a high transmission ratio within the weight limit [8,41,42].

Table 3. Mechanisms commonly used in powered prostheses.

Common Mechanism	Advantages	Drawbacks	
slider-crank	(1) simple mechanism (2) can utilize linear actuator	(1) nonlinear kinematics require more sensors for measurement	[12,16,18,31,35]
four-bar linkage	(1) more parameters can be optimized to achieve enhanced performance (2) more stable structure (3) can utilize linear actuator		[8,13,54–56]
direct drive	(1) can provide the most stable structure (2) can reduce the device size	(1) elastic element design is critical (2) high-torque motor is required	[21,38,41,57] [8] [42]
cable-driven	(1) design can be upgraded to two DoFs system (2) can increase maximum torque generation	(1) nonlinearity and unmodeled elasticity can affect the control behavior (2) sacrifices the design stability	[56–61]

The most critical challenge for robotic prostheses' mechanical systems is the high torque-to-weight ratio required to support the body weight. Therefore, a high efficiency speed reducer with compact design and high reduction ratio is needed. Some recent designs [8] use harmonic gear as the system reducer. However, the selection of the series elastic element is extremely critical to avoid damaging the gear box as a result of repetitive shock loads. Despite the success in utilizing cycloidal gear boxes in machining robots (high torque with direct contact with working environment) [62], a review of the literature illustrates the gap in robotic prostheses design [63]. Therefore, the main objective of this paper is to present a distinguished design of robotic knee prosthesis; in other words, the design is the first robotic prosthesis with a cycloidal gear drive and optimized four-bar mechanism. The optimized four-bar mechanism restricts the robotic knee prosthesis' RoM, which provides structural safety in both passive and active operational modes.

The rest of this paper is arranged as follows: the design methodology is identified in Section 2. Robotic knee prosthesis mechanical design is provided in Section 3. Finally, the conclusion and future work are outlined in Section 4.

2. Method

Cycloid drives are compact high-ratio speed reducers with a reduction ratio around 10:1, which can have an efficiency up to 70 percent [64]. This is due to the friction at the contact points, which is the main source of losses in the cycloid drive [65]. The cycloidal gear efficiency can increase up to 90 percent if roller bearings are placed at the contact points [66]. Utilizing cycloidal gear in robotic prostheses is recommended because of its ability to be back-driven and due to the high torque-to-weight ratio required in the application [67]. A six-step guide line for performance testing is given in [68]; the method can be used to evaluate cycloid drive in high-performance robots and can be edited to assess the robotic knee prosthesis.

The basic method to generate the cycloidal profile is given in [69,70]. The cycloidal profiles (i.e., epitrochoidal and hypotrochoidal) were analyzed extensively in the literature [71]. In this work, the epitrochoidal profile was selected because the overall gear design can give good performance for different performance targets [72].

The PSO algorithm was introduced in [73], which was inspired by bird flocks searching for corn. PSO is widely used in unstructured continuous/discrete, multivariable, constrained and unconstrained optimization problems [74]. Figure 1 illustrates the original PSO algorithm, where i is the number of iterations.

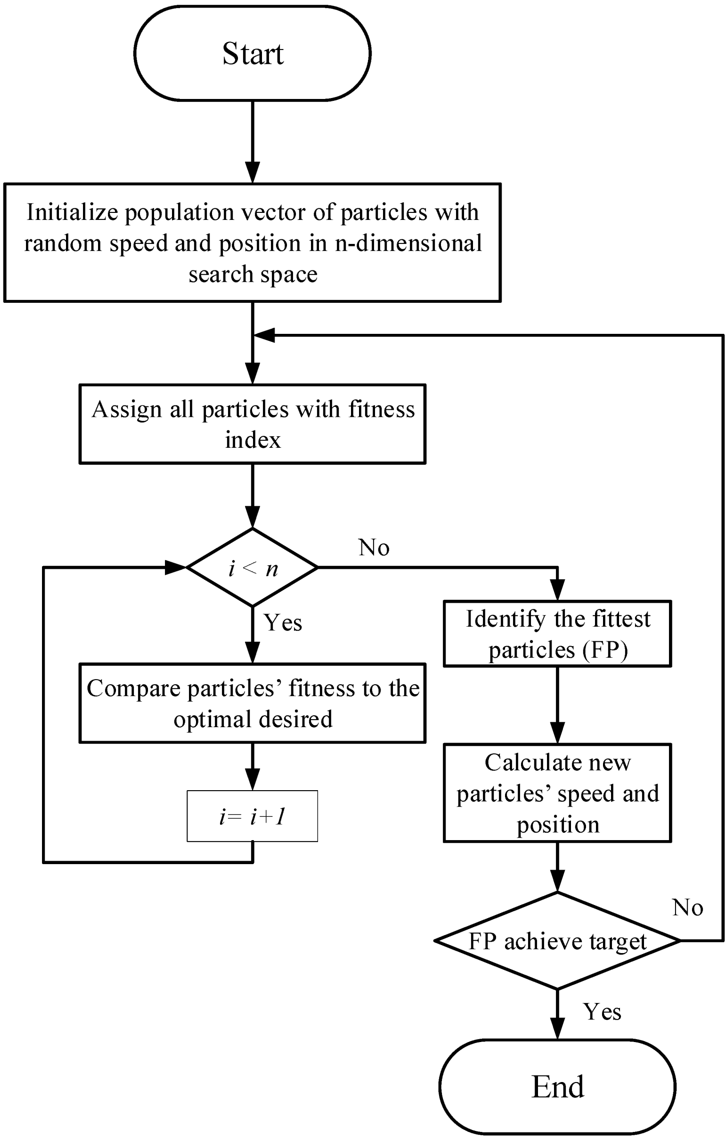

Figure 1. Original PSO algorithm presented in a simplified flowchart.

The PSO was advanced and hybridized with different algorithms to enhance the converging speed and generalization ability [75–77]. In the past decades, the PSO algorithm was implemented to solve multivariable optimization problems and it exhibits good performance [78]. In [79], the authors used PSO to optimize four-bar linkage joint clearance. Several successful prototypes presented in the literature utilized linkage mechanisms to mimic the knee joint [80–83]. Linkage mechanisms were adapted for their ability to produce a nonlinear profile and amplify the input force [84]. To evaluate the mechanism in the proposed robotic knee prosthesis, the four-bar mechanism was evaluated based on the method presented in [85]. The robotic knee prosthesis scheme is outlined in the next section.

3. Mechanical Design for a Robotic Knee Prosthesis

In this section, an outline of the robotic knee prosthesis design and hardware assembly is presented. This section is divided into three subsections: design of cycloidal gear, kinematics analysis of four-bar mechanism, and system assembly. The system utilizes an outrunner BLDC motor because of the compact size and high torque-to-weight ratio; the motor maximum output torque is 0.94 N.m.

3.1. Cycloidal Gear for Robotic Knee Prosthesis

The cycloidal gear is based on an epicycloid, in which the original profile of the cycloid disk is given in [86]. The profile can be given in the Cartesian coordinate system, as shown in Equations (1) and (2), where d is the base circle diameter, ϕ is a free variable that takes value from 0 to 2π, e is the disc eccentricity, n is number of lobes (see Figure 2), ε is the radius of roller, and Γ is the contact angle between lobe and roller. To reduce cycloidal gear vibration, a cycloidal disc pair is designed with a 180 degree shift [87,88]. Figure 2 shows the profile of the cycloid disc with two reference circles.

$$x = \frac{d}{2} \cdot \cos(\phi) + e \cdot \cos(\phi \cdot (n+1)) - \varepsilon \cdot \cos(\phi + \Gamma) \tag{1}$$

$$y = \frac{d}{2} \cdot \sin(\phi) + e \cdot \sin(\phi \cdot (n+1)) - \varepsilon \cdot \sin(\phi + \Gamma) \tag{2}$$

$$\Gamma = arctan\left(\frac{\sin(n \cdot \phi)}{\frac{d}{2ne} + \cos(n \cdot \phi)}\right) \tag{3}$$

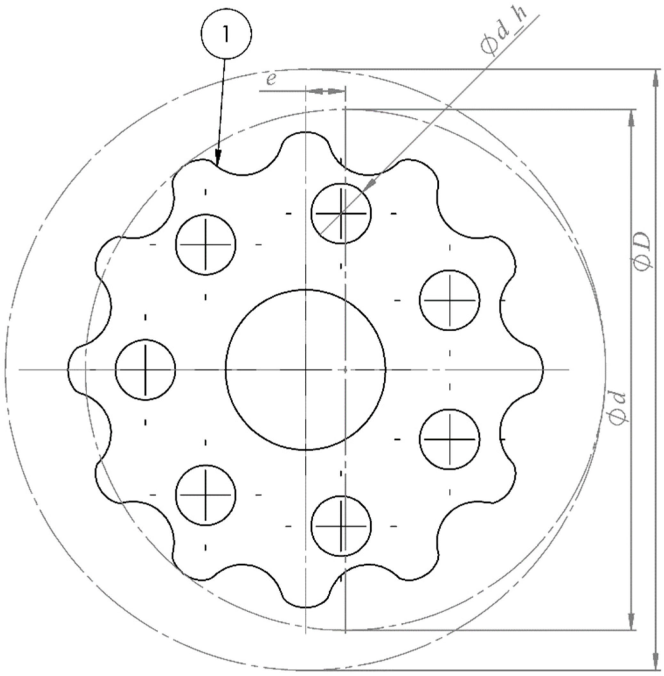

Figure 2. Cycloid disc profile with the important metrics highlighted: e—eccentricity, d_h—hole diameters, D—reference circle diameter of the fixed ring pins, d—base circle diameter, and ① indicates a lobe.

To assure that the system is working at its highest efficiency, the reduction ratio (i) is bound to be smaller than 20 while taking into consideration that the design's torque requirement is around 55 N.m. The first transmission is selected to be i = 12. The maximum actuator output at this stage is approximately 10 N.m, where the cycloidal drive and motor efficiencies are 0.89 and 0.98, respectively. Figure 3 illustrates the assembled system of the BLDC motor and gear.

In Table 4, a complete list of the cycloidal gear parameters and description are provided for reference.

The cycloidal disks were reinforced by continuous carbon fiber to enhance the wear and tear at the contact point by increasing the disk stiffness. The reinforcement is highlighted in blue and illustrated in Figure 4.

Figure 3. Initial assembly of the cycloidal gear drive for testing and load evaluation.

Table 4. Cycloidal gear design parameters.

	Description	Value
d	circle diameter of base circle	50.4 mm
D	reference circle diameter of the fixed ring pins	54.6 mm
N	number of pins	13
n	number of lobes	12
e	eccentricity	4 mm
i	reduction ratio	$\frac{n}{N-n} = 12$
e	roller radius	3.175 mm
d_h	hole diameter	$d_h = 2\ (\varepsilon + e)$ = 14.35 mm

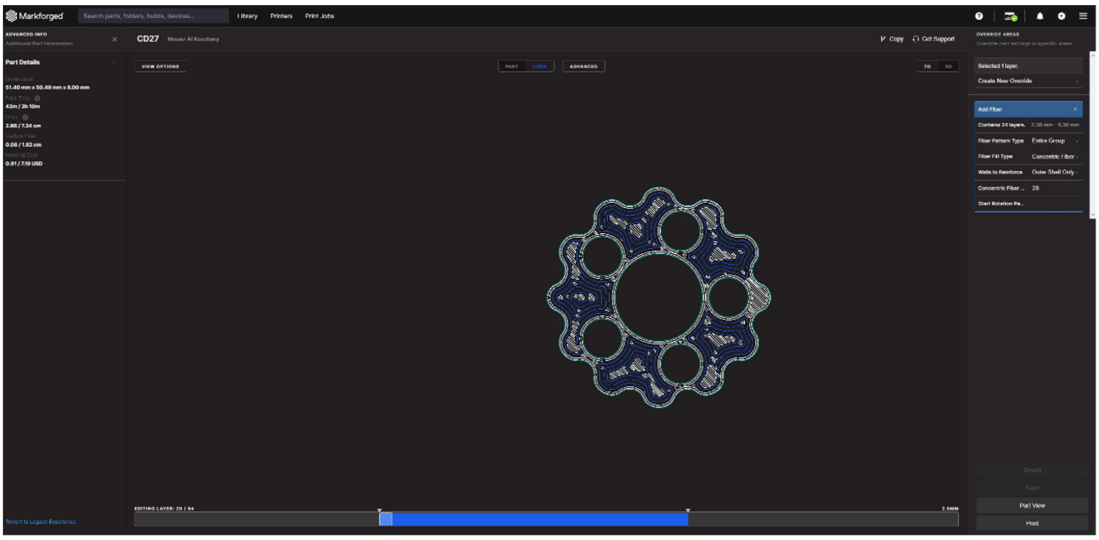

Figure 4. One-layer illustration of carbon-fiber reinforcement of the cycloidal disks.

To link the output shaft to the four-bar linkage input point, a timing belt with a 4:1 reduction ratio is used; the maximum input torque to the four-bar mechanism should be slightly more than 39 N.m.

3.2. Four-Bar Linkage Design and Kinematic Analysis

In this subsection, the design and optimization of the four-bar mechanism is discussed, beginning with the kinematic analysis to the optimization of the linkages, and at last, the output torque calculation.

There are many methods to study the four-bar linkage. The vector representation in complex domain is one of the most effective methods for kinematic analysis. Figure 5 shows a generalized structure of the four-bar mechanism.

$$\vec{r_1} + \vec{r_2} = \vec{r_3} + \vec{r_4}. \tag{4}$$

$$r_1 \times e^{j\theta_s} + r_2 \times e^{j\theta_2} = r_3 \times e^{j\theta_3} + r_4 \times e^{j\theta_0} \tag{5}$$

$$r_1 \times e^{-j\theta_s} + r_2 \times e^{-j\theta_2} = r_3 \times e^{-j\theta_3} + r_4 \times e^{-j\theta_0} \tag{6}$$

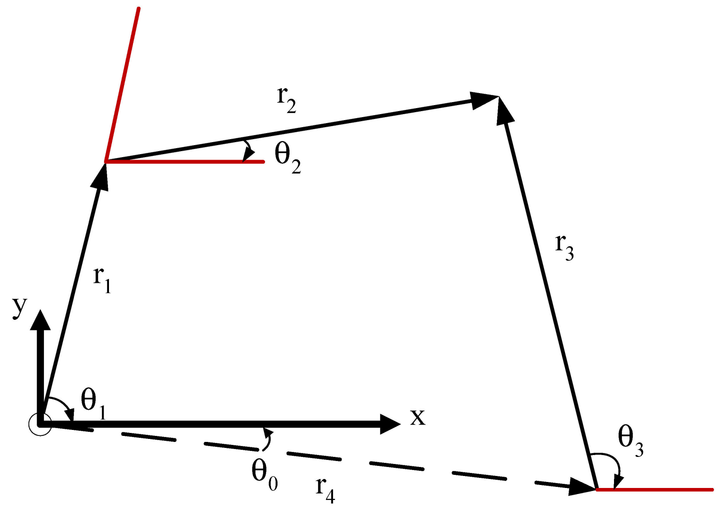

Figure 5. A vector representation of four-bar linkage mechanism. Where the red lines represent reference geometry.

By isolating the vector $\vec{r_3}$ and multiplying Equations (5) and (6), we can find the relation between θ_1 and θ_2:

$$\begin{aligned} r_1^2 + r_2^2 - r_3^2 + r_b^2 + 2 \times r_1 \times r_2 \times \left(C_{\theta_s} \times C_{\theta_2} - S_{\theta_s} \times S_{\theta_2}\right) - 2 \times r_2 \times r_b \\ \times \left(C_{\theta_2} \times C_{\theta_0} - S_{\theta_2} \times S_{\theta_0}\right) - 2 \times r_1 \times r_b \\ \times \left(C_{\theta_s} \times C_{\theta_0} - S_{\theta_s} \times S_{\theta_0}\right) = 0 \end{aligned} \tag{7}$$

$$A_1^* = r_1^2 + r_2^2 - r_3^2 + r_b^2 \tag{8}$$

$$A_2^* = -2 \times r_1 \times r_b \times \left(C_{\theta_s} \times C_{\theta_0} - S_{\theta_s} \times S_{\theta_0}\right) \tag{9}$$

$$B_1^* = 2 \times r_1 \times r_2 \times C_{\theta_s} - 2 \times r_2 \times r_b \times C_{\theta_0} \tag{10}$$

$$B_2^* = 2 \times r_1 \times r_2 \times S_{\theta_s} - 2 \times r_2 \times r_b \times S_{\theta_0} \tag{11}$$

Using half-angle rules, Equation (7) is transformed into a quadratic equation. With the use of the combined variables given in Equations (8)–(11), the final equation can be written, as shown in Equation (12). The parameters of Equation (12) can be rearranged to simplify the equation by combining Equations (12)–(16).

$$(A_1^* + A_2^* - B_1^*) \times T_{\theta_2/2}^2 + 2 \times B_2^* \times T_{\theta_2/2} + A_1^* + A_2^* + B_1^* = 0 \tag{12}$$

$$A = A_1^* + A_2^* - B_1^* \tag{13}$$

$$B = 2 \times B_2^* \tag{14}$$

$$C = A_1^* + A_2^* + B_1^* \tag{15}$$

$$x = T_{\theta_2/2} \tag{16}$$

$$A \times x^2 + B \times x + C = 0 \tag{17}$$

Equation (17) can be solved to find θ_2 (output angle) in terms of θ_s.

$$\theta_2 = 2 \times atan2\left(-B - \sqrt{B^2 - 4 \times A \times C}, 2A\right) \tag{18}$$

Finally, the maximum output torque is given in Equation (19). A full kinetic analysis was derived in [88]. In the early stance-phase, $\theta_2 = 0$ and $\theta_3 = -\pi/2$. Therefore, the maximum torque and the robotic knee prosthesis RoM can be determined by optimizing the bars' lengths.

$$\tau_{out,max} = \frac{r_3}{r_1} \cdot \tau_{in,max} \cdot cos\left(\theta_{2,stance} - \theta_{3,stance} - \frac{\pi}{2}\right) \tag{19}$$

To find the value of the four bars, an objective function is defined by Equation (18) and the target value (Equation (20)). PSO algorithm with restriction is developed to minimize the objective function. The optimization technique was run using MATLAB (2019a). Figure 6 shows the average knee joint RoM for normal walking gait.

$$f_{obj}(r_1, r_2, r_3, r_b, \theta_s) = Knee_{rom} - \theta_2 \tag{20}$$

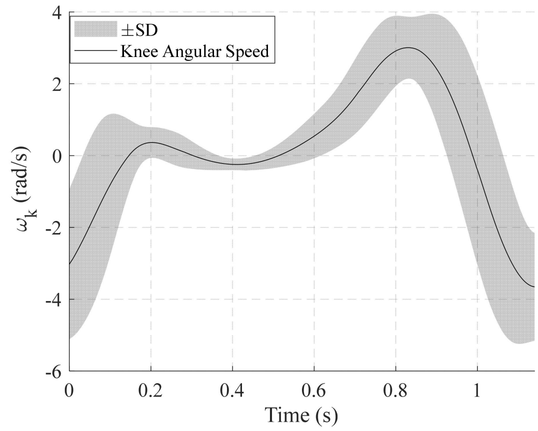

(**a**)

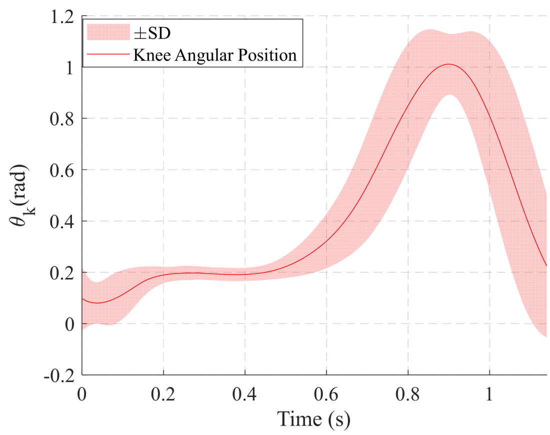

(**b**)

Figure 6. Knee kinematics in the sagittal plane for 50 consecutive steps of a normal subject with a self-selected walking speed. (**a**) The average of knee angular speed is shown in solid black and standard deviation is in gray. (**b**) The average of knee angular position is shown in solid red and standard deviation is in pink.

Using the parameters given in Table 5, Equation (19) yields a maximum torque of 82 N.m (considering bearing efficiency is 0.95). Overall design assembly is illustrated in Figure 7.

Table 5. Four-bar mechanism optimized parameters.

Link	Parameters
r_1	30 mm
r_2	56.624 mm
r_3	66 mm
r_b	66.193 mm
q_0	0.43706 rad

Figure 7. Robotic knee prosthesis design assembly.

4. Conclusions

In this paper, an overview of a robotic knee prosthesis design utilizing cycloidal gear drive and four-bar linkage mechanism is provided. The four-bar linkage mechanism is optimized using the PSO algorithm. The prosthesis developed can provide up to 82 N.m, which can support a 120 kg person; the prototype overall weight is 0.9 Kg, including two pyramid adaptors and a battery.

The current design limitation is the lack of an additional elastic element that can mimic the knee stiffness. A combination of a series of springs is a viable option to fulfill the design requirements of high stiffness during the stance phase and minimum stiffness during the swing phase. The series spiral spring(s) will be designed as we discussed in [88], and will be attached to the actuator. Furthermore, a control system should be established to have the capability to control the robotic knee prosthesis under two modes (i.e., passive and active foot).

Author Contributions: M.A.K.: conceptualization, data collection, data analysis, visualization, computer-aided design, computer-aided manufacturing, software, and original draft writing; H.A.K.: conceptualization, data collection, data analysis, computer-aided manufacturing, and manuscript review and editing; J.L.: data collection, data analysis, computer-aided design, and manuscript review and editing; T.K.: data analysis, visualization, software, and manuscript review and editing; Z.A.-H.: data analysis, visualization, software, and manuscript review and editing; H.N.S.: data collection, visualization, group administration, and manuscript review and editing; N.A.: supervision, data collection, investigation, and manuscript review and editing; N.A.A.O.: supervision, conceptualization, group administration, investigation, and manuscript review and editing. All authors have read and agreed to the published version of the manuscript.

Funding: This work is supported by the Ministry of Science, Technology, and Innovation, Malaysia, under the grant NTIS-Sandbox (grant number: NTIS 098773).

Institutional Review Board Statement: This study was granted approval from the Medical Research and Ethics Committee's (MREC) (reference number: KKM/NIHSEC/P19-2206(11)).

Informed Consent Statement: All subjects agreed to participate in this study by signing a consent form. All subjects gave permission to publish the data collected during the trials by signing a consent form.

Data Availability Statement: All data generated during this work are available in the manuscript; additional data are available upon reasonable request from the corresponding author.

Acknowledgments: The authors acknowledge Ministry of Science, Technology, and Innovation, Malaysia (MTDC) funds for this work, under the grant NTIS-Sandbox: (grant number: NTIS 098773).

Conflicts of Interest: The authors have no conflict of interest.

References

1. Levangie, P.K.; Norkin, C.C. *Joint Structure and Function: A Comprehensive Analysis*; F.A. Davis: Philadelphia, PA, USA, 2011.
2. Hamill, J.; Knutzen, K.M. *Biomechanical Basis of Human Movement*; Lippincott Williams & Wilkins: Philadelphia, PA, USA, 2006.
3. Muller, M.D. *Transfemoral Amputation: Prosthetic Management. Atlas of Amputations and Limb Deficiencies*, 4th ed.; American Academy of Orthopaedic Surgeons: Rosemont, IL, USA, 2016; pp. 537–554.
4. Melfi, M.J.; Evon, S.; McElveen, R. Induction versus permanent magnet motors. *IEEE Ind. Appl. Mag.* **2009**, *15*, 28–35. [CrossRef]
5. Hameyer, K.; Belmans, R.J. Permanent magnet excited brushed DC motors. *IEEE Trans. Ind. Electron.* **1996**, *43*, 247–255. [CrossRef]
6. Derammelaere, S.; Haemers, M.; De Viaene, J.; Verbelen, F.; Stockman, K. A quantitative comparison between BLDC, PMSM, brushed DC and stepping motor technologies. In Proceedings of the 2016 19th International Conference on Electrical Machines and Systems (ICEMS), Chiba, Japan, 13–16 November 2016; pp. 1–5.
7. Carney, M.E.; Shu, T.; Stolyarov, R.; Duval, J.-F.; Herr, H.M. Design and Preliminary Results of a Reaction Force Series Elastic Actuator for Bionic Knee and Ankle Prostheses. *IEEE Trans. Med Robot. Bionics* **2021**, *3*, 542–553. [CrossRef]
8. Azocar, A.F.; Mooney, L.M.; Duval, J.-F.; Simon, A.M.; Hargrove, L.J.; Rouse, E.J. Design and clinical implementation of an open-source bionic leg. *Nat. Biomed. Eng.* **2020**, *4*, 941–953. [CrossRef]
9. Au, S.K.; Dilworth, P.; Herr, H. An ankle-foot emulation system for the study of human walking biomechanics. In Proceedings of the 2006 IEEE International Conference on 2006, Orlando, FL, USA, 15–19 May 2006; pp. 2939–2945.
10. Au, S.K.; Herr, H.; Weber, J.; Martinez-Villalpando, E.C. Powered ankle-foot prosthesis for the improvement of amputee ambulation. In Proceedings of the 2007 29th Annual International Conference of the IEEE Engineering in Medicine and Biology Society, Lyon, France, 22–26 August 2007; pp. 3020–3026.
11. Au, S.K.; Herr, H.M. Powered ankle-foot prosthesis. *IEEE Robot. Autom. Mag.* **2008**, *15*, 52–59. [CrossRef]
12. Eilenberg, M.F.; Geyer, H.; Herr, H. Control of a Powered Ankle–Foot Prosthesis Based on a Neuromuscular Model. *IEEE Trans. Neural Syst. Rehabil. Eng.* **2010**, *18*, 164–173. [CrossRef] [PubMed]
13. Hsieh, T.-H. Design and Control of a Two-Degree-of-Freedom Powered Ankle-Foot Prosthesis. Master's Thesis, Massachusetts Institute of Technology, Massachusetts Ave, Cambridge, MA, USA, 2019.
14. Hitt, J.K.; Bellman, R.; Holgate, M.; Sugar, T.G.; Hollander, K.W. The sparky (spring ankle with regenerative kinetics) project: Design and analysis of a robotic transtibial prosthesis with regenerative kinetics. In Proceedings of the International Design Engineering Technical Conferences and Computers and Information in Engineering Conference, Las Vegas, NV, USA, 4–7 September 2007; pp. 1587–1596.
15. Holgate, M.A.; Hitt, J.K.; Bellman, R.D.; Sugar, T.G.; Hollander, K.W. The SPARKy (Spring Ankle with Regenerative kinetics) project: Choosing a DC mo-tor based actuation method. In Proceedings of the 2008 2nd IEEE RAS & EMBS International Conference on Biomedical Robotics and Biomechatronics, Scottsdale, AZ, USA, 19–22 October 2008; pp. 163–168.
16. Zhu, J.; Wang, Q.; Wang, L. PANTOE 1: Biomechanical design of powered ankle-foot prosthesis with compliant joints and segmented foot. In Proceedings of the Advanced Intelligent Mechatronics (AIM), 2010 IEEE/ASME International Conference on 2010, Montreal, QC, Canada, 6–9 July 2010; pp. 31–36.
17. Wang, Q.; Yuan, K.; Zhu, J.; Wang, L. Finite-state control of a robotic transtibial prosthesis with motor-driven nonlinear damping behaviors for level ground walking. In Proceedings of the Advanced Motion Control (AMC), 2014 IEEE 13th International Workshop on 2014, Yokohama, Japan, 14–16 March 2014; pp. 155–160.
18. Wang, Q.; Yuan, K.; Zhu, J.; Wang, L. Walk the Walk: A Lightweight Active Transtibial Prosthesis. *IEEE Robot. Autom. Mag.* **2015**, *22*, 80–89. [CrossRef]
19. Feng, Y.; Zhu, J.; Wang, Q. Metabolic cost of level-ground walking with a robotic transtibial prosthesis combining push-off power and nonlinear damping behaviors: Preliminary results. In Proceedings of the Engineering in Medicine and Biology Society (EMBC), 2016 IEEE 38th Annual International Conference of the 2016, Orlando, FL, USA, 16–20 August 2016; pp. 5063–5066.
20. Shultz, A.H.; Mitchell, J.E.; Truex, D.; Lawson, B.E.; Goldfarb, M. Preliminary evaluation of a walking controller for a powered ankle prosthesis. In Proceedings of the Robotics and Automation (ICRA), 2013 IEEE International Conference on 2013, Montreal, QC, Canada, 4 October 2013; pp. 4838–4843.
21. Shultz, A.H.; Lawson, B.E.; Goldfarb, M. Variable Cadence Walking and Ground Adaptive Standing With a Powered Ankle Prosthesis. *IEEE Trans. Neural Syst. Rehabil. Eng.* **2015**, *24*, 495–505. [CrossRef]

22. Sun, J.; Voglewede, P.A. Controller implementation of a powered transtibial prosthetic device. In Proceedings of the ASME 2011 International Design Engineering Technical Conferences and Computers and Information in Engineering Conference, Washington, DC, USA, 28–31 August 2011; pp. 597–603.
23. LaPre, A.K.; Umberger, B.R.; Sup, F.C. A Robotic Ankle–Foot Prosthesis With Active Alignment. *J. Med. Devices* **2016**, *10*, 025001. [CrossRef]
24. Cherelle, P.; Matthys, A.; Grosu, V.; Vanderborght, B.; Lefeber, D. The AMP-Foot 2.0: Mimicking intact ankle behavior with a powered transtibial prosthe-sis. In Proceedings of the Biomedical Robotics and Biomechatronics (BioRob), 2012 4th IEEE RAS & EMBS International Conference on 2012, Rome, Italy, 24–27 June 2012; pp. 544–549.
25. Cherelle, P.; Grosu, V.; Matthys, A.; Vanderborght, B.; Lefeber, D. Design and validation of the ankle mimicking prosthetic (AMP-) foot 2.0. *IEEE Trans. Neural Syst. Rehabil. Eng.* **2014**, *22*, 138–148. [CrossRef]
26. Cherelle, P.; Grosu, V.; Cestari, M.; Vanderborght, B.; Lefeber, D. The AMP-Foot 3, new generation propulsive prosthetic feet with explosive motion char-acteristics: Design and validation. *Biomed. Eng. Online* **2016**, *15*, 21. [CrossRef] [PubMed]
27. Jimenez-Fabian, R.; Flynn, L.; Geeroms, J.; Vitiello, N.; VanderBorght, B.; Lefeber, D. Sliding-Bar MACCEPA for a Powered Ankle Prosthesis. *J. Mech. Robot.* **2015**, *7*, 041011. [CrossRef]
28. Jimenez-Fabian, R.; Geeroms, J.; Flynn, L.; Vanderborght, B.; Lefeber, D. Reduction of the torque requirements of an active ankle prosthesis using a parallel spring. *Robot. Auton. Syst.* **2017**, *92*, 187–196. [CrossRef]
29. Gao, F.; Liu, Y.; Liao, W.-H. A new powered ankle-foot prosthesis with compact parallel spring mechanism. In Proceedings of the Robotics and Biomimetics (ROBIO), 2016 IEEE International Conference on 2016, Liege, Belgium, 13–14 December 2016; pp. 473–478.
30. Gao, F.; Liu, Y.; Liao, W.-H. Implementation and Testing of Ankle-Foot Prosthesis With a New Compensated Controller. *IEEE/ASME Trans. Mechatron.* **2019**, *24*, 1775–1784. [CrossRef]
31. Grimmer, M.; Holgate, M.; Holgate, R.; Boehler, A.; Ward, J.; Hollander, K.; Sugar, T.; Seyfarth, A. A powered prosthetic ankle joint for walking and run-ning. *Biomed. Eng. Online* **2016**, *15*, 37–52. [CrossRef]
32. Alleva, S.; Antonelli, M.G.; Zobel, P.B.; Durante, F. Biomechanical Design and Prototyping of a Powered Ankle-Foot Prosthesis. *Materials* **2020**, *13*, 5806. [CrossRef]
33. Dong, D.; Ge, W.; Convens, B.; Sun, Y.; Verstraten, T.; Vanderborght, B. Design, Optimization and Energetic Evaluation of an Efficient Fully Powered An-kle-Foot Prosthesis With a Series Elastic Actuator. *IEEE Access* **2020**, *8*, 61491–61503. [CrossRef]
34. She, H.; Zhu, J.; Tian, Y.; Wang, Y.; Huang, Q. Design of a powered ankle-foot prosthesis with an adjustable stiffness toe joint. *Adv. Robot.* **2020**, *34*, 689–697. [CrossRef]
35. Sup, F.; Varol, H.A.; Mitchell, J.; Withrow, T.J.; Goldfarb, M. Preliminary Evaluations of a Self-Contained Anthropomorphic Transfemoral Prosthesis. *IEEE/ASME Trans. Mechatron.* **2009**, *14*, 667–676. [CrossRef]
36. Martinez-Villalpando, E.C.; Herr, H. Agonist-antagonist active knee prosthesis: A preliminary study in level-ground walking. *J. Rehabil. Res. Dev.* **2009**, *46*, 46. [CrossRef]
37. Rouse, E.J.; Mooney, L.M.; Martinez-Villalpando, E.C.; Herr, H.M. Clutchable series-elastic actuator: Design of a robotic knee prosthesis for minimum energy consumption. In Proceedings of the 2013 IEEE 13th International Conference on Rehabilitation Robotics (ICORR), Beijing, China, 15–18 July 2013; pp. 1–6.
38. Shultz, A.H.; Lawson, B.E.; Goldfarb, M. Running with a powered knee and ankle prosthesis. *IEEE Trans. Neural Syst. Rehabil. Eng.* **2014**, *23*, 403–412. [CrossRef] [PubMed]
39. Rouse, E.J.; Mooney, L.M.; Herr, H.M. Clutchable series-elastic actuator: Implications for prosthetic knee design. *Int. J. Robot. Res.* **2014**, *33*, 1611–1625. [CrossRef]
40. Zhao, H.; Reher, J.; Horn, J.; Paredes, V.; Ames, A.D. Realization of nonlinear real-time optimization based controllers on self-contained transfemoral prosthesis. In Proceedings of the ACM/IEEE Sixth International Conference on Cyber-Physical Systems, Seattle, DC, USA, 14–16 April 2015; pp. 130–138.
41. Zhao, H.; Ambrose, E.; Ames, A.D. Preliminary results on energy efficient 3D prosthetic walking with a powered compliant transfemoral prosthesis. In Proceedings of the 2017 IEEE International Conference on Robotics and Automation (ICRA), Brussels, Belgium, 11–12 December 2017; pp. 1140–1147.
42. Elery, T.; Rezazadeh, S.; Nesler, C.; Gregg, R.D. Design and validation of a powered knee–ankle prosthesis with high-torque, low-impedance actuators. *IEEE Trans. Robot.* **2020**, *36*, 1649–1668. [CrossRef] [PubMed]
43. Flynn, L.; Geeroms, J.; Jimenez-Fabian, R.; Heins, S.; Vanderborght, B.; Munih, M.; Molino Lova, R.; Vitiello, N.; Lefeber, D. The challenges and achieve-ments of experimental implementation of an active transfemoral prosthesis based on biological quasi-stiffness: The CYBERLEGs beta-prosthesis. *Front. Neurorobotics* **2018**, *12*, 80. [CrossRef]
44. Hong, W.; Paredes, V.; Chao, K.; Patrick, S.; Hur, P. Consolidated control framework to control a powered transfemoral prosthesis over inclined terrain conditions. In Proceedings of the 2019 International Conference on Robotics and Automation (ICRA), Montreal, QC, Canada, 20–24 May 2019; pp. 2838–2844.
45. Lenzi, T.; Cempini, M.; Hargrove, L.; Kuiken, T. Design, development, and testing of a lightweight hybrid robotic knee prosthesis. *Int. J. Robot. Res.* **2018**, *37*, 953–976. [CrossRef]
46. Liu, J.; Osman, N.A.A.; Kouzbary, M.A.; Kouzbary, H.A.; Razak, N.A.A.; Shasmin, H.N.; Arifin, N. Optimization and comparison of typical elastic actuators in powered ankle-foot prosthesis. *Int. J. Control. Autom. Syst.* **2022**, *20*, 232–242. [CrossRef]
47. Hedrick, E.A.; Malcolm, P.; Wilken, J.M.; Takahashi, K.Z. The effects of ankle stiffness on mechanics and energetics of walking with added loads: A pros-thetic emulator study. *J. Neuroeng. Rehabil.* **2019**, *16*, 1–15. [CrossRef]

48. Clites, T.R.; Shepherd, M.K.; Ingraham, K.A.; Wontorcik, L.; Rouse, E.J. Understanding patient preference in prosthetic ankle stiffness. *J. Neuroeng. Rehabil.* **2021**, *18*, 1–16. [CrossRef]
49. Quesada, R.E.; Caputo, J.M.; Collins, S.H. Increasing ankle push-off work with a powered prosthesis does not necessarily reduce metabolic rate for tran-stibial amputees. *J. Biomech.* **2016**, *49*, 3452–3459. [CrossRef]
50. Burgess, S.C. A review of linkage mechanisms in animal joints and related bio-inspired designs. *Bioinspiration Biomim* **2021**, *16*, 041001. [CrossRef]
51. Kim, S.I.; Kim, Y.Y. Topology optimization of planar linkage mechanisms. *Int. J. Numer. Methods Eng.* **2014**, *98*, 265–286. [CrossRef]
52. Sup, F.; Bohara, A.; Goldfarb, M. Design and Control of a Powered Transfemoral Prosthesis. *Int. J. Robot. Res.* **2008**, *27*, 263–273. [CrossRef] [PubMed]
53. Sun, J.; Voglewede, P.A. Powered transtibial prosthetic device control system design, implementation, and bench testing. *J. Med. Devices* **2014**, *8*, 011004. [CrossRef]
54. Sun, J.; Fritz, J.M.; Del Toro, D.R.; Voglewede, P.A. Amputee Subject Testing Protocol, Results, and Analysis of a Powered Transtibial Prosthetic Device. *J. Med Devices* **2014**, *8*, 041007–410076. [CrossRef] [PubMed]
55. Zhao, H.; Reher, J.; Horn, J.; Paredes, V.; Ames, A.D. Realization of stair ascent and motion transitions on prostheses utilizing optimization-based control and intent recognition. In Proceedings of 2015 IEEE International Conference on Rehabilitation Robotics (ICORR), Singapore, 11–14 August 2015; pp. 265–270.
56. Au, S.K.; Weber, J.; Herr, H. Biomechanical design of a powered ankle-foot prosthesis. In Proceedings of the 2007 IEEE 10th International Conference on Rehabilitation robotics, Noordwijk, The Netherlands, 13–15 June 2007; pp. 298–303.
57. Ficanha, E.M.; Rastgaar, M.; Kaufman, K.R. A two-axis cable-driven ankle-foot mechanism. *Robot. Biomim.* **2014**, *1*, 379. [CrossRef]
58. Caputo, J.M.; Collins, S.H. An experimental robotic testbed for accelerated development of ankle prostheses. In Proceedings of the 2013 IEEE International Conference on Robotics and Automation, Karlsruhe, Germany, 6–10 May 2013; pp. 2645–2650.
59. Caputo, J.M.; Collins, S.H. A Universal Ankle–Foot Prosthesis Emulator for Human Locomotion Experiments. *J. Biomech. Eng.* **2014**, *136*, 035002. [CrossRef]
60. Pham, A.-D.; Ahn, H.-J. Rigid precision reducers for machining industrial robots. *Int. J. Precis. Eng. Manuf.* **2021**, *22*, 1469–1486. [CrossRef]
61. Lara-Barrios, C.M.; Blanco-Ortega, A.; Guzmán-Valdivia, C.H.; Valles, K.D.B. Literature review and current trends on transfemoral powered prosthetics. *Adv. Robot.* **2017**, *32*, 51–62. [CrossRef]
62. Sensinger, J.W. Efficiency of high-sensitivity gear trains, such as cycloid drives. *J. Mech. Des.* **2013**, *135*, 071006. [CrossRef]
63. Blagojevic, M.; Kocic, M.; Marjanovic, N.; Stojanovic, B.; Dordevic, Z.; Ivanovic, L.; Marjanovic, V. Influence of the friction on the cycloidal speed reducer efficiency. *J. Balk. Tribol. Assoc.* **2012**, *18*, 217–227.
64. Lee, K.; Hong, S.; Oh, J.-H. Development of a Lightweight and High-efficiency Compact Cycloidal Reducer for Legged Robots. *Int. J. Precis. Eng. Manuf.* **2019**, *21*, 415–425. [CrossRef]
65. Sensinger, J.W.; Lipsey, J.H. Cycloid vs. harmonic drives for use in high ratio, single stage robotic transmissions. In Proceedings of the 2012 IEEE International Conference on Robotics and Automation, St Paul, MN, USA, 14–18 May 2012; pp. 4130–4135.
66. Qiu, Z.; Xue, J. Review of Performance Testing of High Precision Reducers for Industrial Robots. *Measurement* **2021**, *183*, 109794. [CrossRef]
67. Botsiber, D.; Kingston, L. Design and performance of the cycloid speed reducer. *Mach. Des.* **1956**, *28*, 65–69.
68. Malhotra, S.; Parameswaran, M. Analysis of a cycloid speed reducer. *Mech. Mach. Theory* **1983**, *18*, 491–499. [CrossRef]
69. Hsieh, C.-F. Study on Geometry Design of Rotors Using Trochoidal Curve. Ph.D. Dissertation, Department of Mechanical Engineering, National Chung Cheng University, Chiayi, Taiwan, 2006.
70. Robison, A.J.; Vacca, A. Performance comparison of epitrochoidal, hypotrochoidal, and cycloidal gerotor gear profiles. *Mech. Mach. Theory* **2021**, *158*, 104228. [CrossRef]
71. Kennedy, J.; Eberhart, R. Particle swarm optimization. In Proceedings of the ICNN′95-International Conference on Neural Networks, Perth, WA, Australia, 27 November–1 December 1995; pp. 1942–1948.
72. Sengupta, S.; Basak, S.; Peters, R.A. Particle Swarm Optimization: A Survey of Historical and Recent Developments with Hybridization Perspectives. *Mach. Learn. Knowl. Extr.* **2018**, *1*, 157–191. [CrossRef]
73. Robinson, J.; Sinton, S.; Rahmat-Samii, Y. Particle swarm, genetic algorithm, and their hybrids: Optimization of a profiled corrugated horn antenna. In Proceedings of the IEEE Antennas and Propagation Society International Symposium (IEEE Cat. No. 02CH37313), San Antonio, TX, USA, 16–21 June 2002; pp. 314–317.
74. Abdel-Kader, R.F. Genetically improved PSO algorithm for efficient data clustering. In Proceedings of the 2010 Second International Conference on Machine Learning and Computing, Bangalore, India, 9–11 February 2010; pp. 71–75.
75. Das, S.; Abraham, A.; Konar, A. Particle Swarm Optimization and Differential Evolution Algorithms: Technical Analysis, Applications and Hybridization Perspectives. In *Advances of Computational Intelligence in Industrial Systems*; Springer: Berlin/Heidelberg, Germany, 2008; Volume 116.
76. Wang, D.; Tan, D.; Liu, L. Particle swarm optimization algorithm: An overview. *Soft Comput.* **2018**, *22*, 387–408. [CrossRef]
77. Sardashti, A.; Daniali, H.M.; Varedi, S.M. Optimal free-defect synthesis of four-bar linkage with joint clearance using PSO algorithm. *Meccanica* **2013**, *48*, 1681–1693. [CrossRef]
78. Sun, Y.; Ge, W.; Zheng, J.; Dong, D. Design and Evaluation of a Prosthetic Knee Joint Using the Geared Five-Bar Mechanism. *IEEE Trans. Neural Syst. Rehabil. Eng.* **2015**, *23*, 1031–1038. [CrossRef]

79. Steele, A.G.; Hunt, A.; Etoundi, A.C. Development of a bio-inspired knee joint mechanism for a bipedal robot. In Proceedings of the Conference on Biomimetic and Biohybrid Systems, Stanford, CA, USA, 26–28 July 2017; pp. 418–427.
80. Jin, D.; Zhang, R.; O Dimo, H.; Wang, R.; Zhang, J. Kinematic and dynamic performance of prosthetic knee joint using six-bar mechanism. *J. Rehabil. Res. Dev.* **2003**, *40*, 39. [CrossRef] [PubMed]
81. Radcliffe, C. Four-bar linkage prosthetic knee mechanisms: Kinematics, alignment and prescription criteria. *Prosthet. Orthot. Int.* **1994**, *18*, 159–173. [CrossRef]
82. Patek, S.N.; Nowroozi, B.; Baio, J.; Caldwell, R.L.; Summers, A.P. Linkage mechanics and power amplification of the mantis shrimp's strike. *J. Exp. Biol.* **2007**, *210*, 3677–3688. [CrossRef] [PubMed]
83. Lin, C.-C.; Chang, W.-T. The force transmissivity index of planar linkage mechanisms. *Mech. Mach. Theory* **2002**, *37*, 1465–1485. [CrossRef]
84. Braren, R. Cycloidal Gears. US Patent US4050331A, 27 September 1977.
85. Heyer, J.H. *Design of Silent, Miniature, High Torque Actuators*; Massachusetts Institute of Technology: Cambridge, MA, USA, 1999.
86. Lin, W.-S.; Shih, Y.-P.; Lee, J.-J. Design of a two-stage cycloidal gear reducer with tooth modifications. *Mech. Mach. Theory* **2014**, *79*, 184–197. [CrossRef]
87. Rothenhofer, G.; Walsh, C.; Slocum, A. Transmission ratio based analysis and robust design of mechanisms. *Precis. Eng.* **2010**, *34*, 790–797. [CrossRef]
88. Liu, J.; Abu Osman, N.A.; Al Kouzbary, M.; Al Kouzbary, H.; Razak, N.A.A.; Shasmin, H.N.; Arifin, N. Stiffness estimation of planar spiral spring based on Gaussian process regression. *Sci. Rep.* **2022**, *12*, 1–15. [CrossRef] [PubMed]